The Astrophysical Journal, 893:125 (13pp), 2020 April 20 https://doi.org/10.3847/1538-4357/ab8223

Scattering-induced Intensity Reduction: Large Mass Content with Small Grains in the Inner Region of the TW Hya disk

Takahiro Ueda, Akimasa Kataoka, and Takashi Tsukagoshi
National Astronomical Observatory of Japan, Osawa 2-21-1, Mitaka, Tokyo 181-8588, Japan; takahiro.ueda@nao.ac.jp
Received 2019 September 16; revised 2020 March 17; accepted 2020 March 19; published 2020 April 23

Abstract

Dust continuum observation is one of the best methods to constrain the properties of protoplanetary disks. Recent theoretical studies have suggested that dust scattering at the millimeter wavelength potentially reduces the observed intensity, which results in an underestimate in the dust mass. We investigate whether dust scattering indeed reduces the observed continuum intensity by comparing the ALMA archival data of the TW Hya disk at Bands 3, 4, 6, 7, and 9 to models obtained by radiative transfer simulations. We find that the model with scattering by 300 μm-sized grains well reproduces the observed spectral energy distribution of the central part of the TW Hya disk while the model without scattering is also consistent within the errors of the absolute fluxes. To explain the intensity at Band 3, the dust surface density needs to be $\sim$10 g cm^{-2} at 10 au in the model with scattering, which is 26 times more massive than previously predicted. The model without scattering needs a 2.3 times higher dust mass than the model with scattering because it needs a lower temperature. At Band 7, scattering reduces the intensity by $\sim$35%, which makes the disk look optically thin even though it is optically thick. Our study suggests the TW Hya disk is still capable of forming cores of giant planets at locations analogous to where the current solar system planets exist.

Unified Astronomy Thesaurus concepts: Planet formation (1241); Protoplanetary disks (1300); Dust continuum emission (412)

1. Introduction

(Sub)Millimeter continuum observations have allowed us to examine the properties of protoplanetary disks. From the continuum emission, the dust mass can be estimated for a given dust opacity and temperature, assuming that the disk is optically thin (Beckwith et al. 1990; Andrews & Williams 2005; Andrews et al. 2013; Ansdell et al. 2016; Cieza et al. 2019). Furthermore, if we look at a disk with multiwavelength observations, the spectral slope of the intensity allows us to estimate the dust size (e.g., Calvet et al. 2002; Draine 2006). However, if the disk is optically thick, it is hard to obtain the information about the dust disk below the photosphere. Even though the inner region where the current solar system planets exist ($\lesssim$30 au) is of the most importance in understanding how solar system analogs form, the inner region of disks would be optically thick at (sub)millimeter wavelengths, since protoplanetary disks are supposed to have a higher surface density at more inner radii (e.g., Lynden-Bell & Pringle 1974; Hayashi 1981).

However, the recent high angular resolution observations from the Disk Substructures at High Angular Resolution Project (DSHARP; Andrews et al. 2018) revealed that most of the DSHARP disks have optical depths less than unity even in the inner region (Huang et al. 2018b). One explanation for these low observed optical depths is the self-scattering of the thermal emission from dust grains (Birnstiel et al. 2018; Carrasco-González et al. 2019; Liu 2019; Zhu et al. 2019; see also Appendix C in Miyake & Nakagawa 1993). Zhu et al. (2019) showed that if the disk is optically thick, dust scattering may reduce the observed optical depth by orders of magnitude, and the disk looks optically thin even if the true optical depth is sufficiently larger than unity. This is because scattering makes the effective free path of emitted photons shorter than that without scattering so that we can only see the upper layer of the disk.

Dust scattering also affects the spectral index α by reducing the observed intensity (Liu 2019; Zhu et al. 2019). The spectral index α is a power-law index of the intensity I as a function of the frequency ν, which has a value higher than 2 for the optically thin disk and as low as 2 for the optically thick disk in the Rayleigh–Jeans limit. However, some disks have shown spectral indices anomalously lower than 2 (e.g., Nomura et al. 2016; Tsukagoshi et al. 2016; Liu et al. 2017; Huang et al. 2018a; Dent et al. 2019). Liu (2019) demonstrated that the optically thick disk can have a spectral index lower than 2 at millimeter wavelengths because of the intensity reduction by scattering, and they showed that it would account for the low spectral index in the inner region of the TW Hya disk reported by Tsukagoshi et al. (2016).

Recent ALMA polarimetric observations have shown that dust scattering indeed occurs in some disks (Kataoka et al. 2016a, 2016b; Bacciotti et al. 2018; Hull et al. 2018; Ohashi et al. 2018; Dent et al. 2019). The polarization caused by dust scattering shows the polarization pattern where the polarization vector is parallel to the minor axis of the disk. From the polarization degree at the observing wavelength, we can put a constrain on the dust size since the scattering behavior is sensitive to the ratio of the dust size to the observing wavelength λ (Kataoka et al. 2015). These observations indicate that dust scattering might affect not only the polarization morphology but also the intensity of the continuum emission.

In this paper, we analyze the ALMA archive data of the continuum observations of the TW Hya disk at Bands 3, 4, 6, 7, and 9 to investigate whether dust scattering indeed affects the observed intensity in the inner region of the disk. In Section 2, we analyze the ALMA archive data and show that the intensities at Bands 7 and 9 are lower than the intensity extrapolated from longer wavelengths with a spectral slope of 2. In Section 3, we perform radiative transfer simulations and demonstrate that the observed Spectral Energy Distribution (SED) is well explained by the model with 300 μm-sized grains that includes scattering. The properties of the inner region of

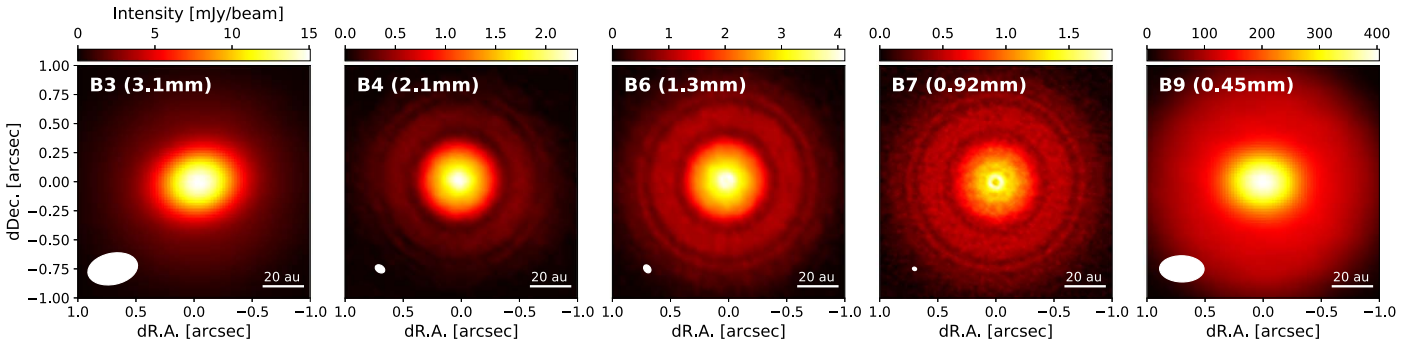

Figure 1. ALMA continuum images of the TW Hya disk at Bands 3, 4, 6, 7, and 9 from left to right. The synthesized beam sizes at Bands 3, 4, 6, 7, and 9 are 0.43 × 0.27, 0.088 × 0.062, 0.075 × 0.055, 0.036 × 0.029, and 0.38 × 0.″23, respectively.

the TW Hya disk are discussed in Section 4, and the summary is presented in Section 5.

2. Millimeter SED of the Central Part of the TW Hya Disk

We investigate the multiwavelength observations of the inner part of the TW Hya disk where previous studies have suggested that it is optically thick at Bands 4 and 6 (e.g., Tsukagoshi et al. 2016). Because the lowest spatial resolution in our data set (∼20 au, corresponding to ∼0.″34) is not high enough to discuss the detailed radial structures, we investigate the SED of the central part of the disk as shown in the following sections.

2.1. ALMA Data and Analysis

In this study, we analyze the public images of the continuum emission of the TW Hya disk at Bands 3, 4, 6, 7, and 9 taken with ALMA. The Band 4 and 6 images are adopted from Tsukagoshi et al. (2016), and the Band 7 image is from Tsukagoshi et al. (2019). For the detailed calibration process of Band 4, 6, and 7 images, we refer readers to Tsukagoshi et al. (2016, 2019). For the Band 3 and 9 images, we downloaded the product images provided by ALMA from the ALMA data archive system (2016.1.00229.S and 2012.1.00422.S, PI: Edwin Bergin). The observed visibilities were reduced and calibrated using the Common Astronomical Software Application (CASA) package (McMullin et al. 2007). The initial flagging of the visibilities and the calibrations for the bandpass characteristics, complex gain, and flux scaling were performed using the pipeline scripts provided by ALMA. After flagging the bad data, the corrected data were concatenated and imaged by CLEAN. The CLEAN map was created by adopting Briggs weighting with a robust parameter of 0.8 for Band 3 and 0.5 for Band 9. After that, self-calibration was applied for the data set.

Figure 1 shows the continuum images of the TW Hya disk at each band. The angular resolution of each observation is 0.43 × 0.27, 0.088 × 0.062, 0.075 × 0.055, 0.036 × 0.029, and 0.38 × 0.″23 for Bands 3, 4, 6, 7, and 9, respectively. Owing to the high spatial resolution, the images at Bands 4, 6, and 7 clearly show the concentric ring and gap-like structures, which have been already reported (e.g., Andrews et al. 2016; Tsukagoshi et al. 2016). In contrast, the Band 3 and 9 images have low angular resolution so that the substructures are not seen. The maximum recoverable scale of the obtained data is 5.″0, 18″, 12″, 8.″8, and 5.″1 for Bands 3, 4, 6, 7, and 9, respectively. Since the diameter of the dust disk around TW Hya is ∼140 au, corresponding to an angular scale of ∼2.″3, our data sufficiently recovers the whole disk emission.

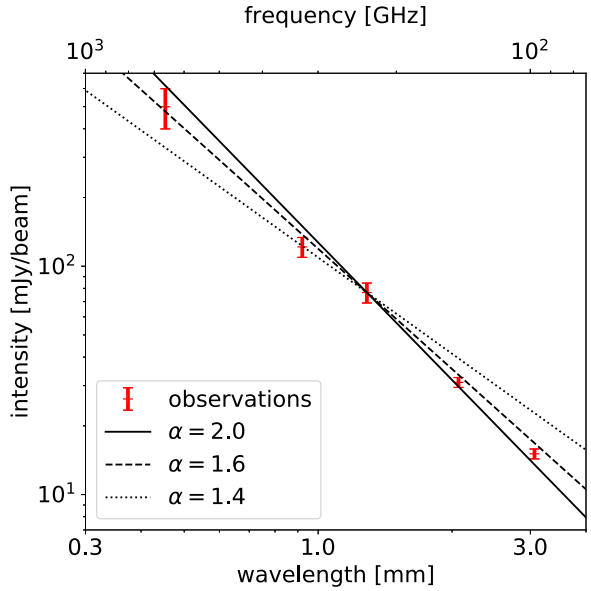

Figure 2. Intensities at the center of the re-convolved images at different observing wavelengths. For reference, the intensity profiles following the spectral indexes of 2, 1.6, and 1.4 are denoted by the solid, dashed, and dotted lines, respectively. The uncertainty in the absolute intensity is set to be 5% for Bands 3 and 4, 10% for Bands 6 and 7, and 20% for Band 9.

2.2. SED Analysis

We focus only on the inner region within the radial distance of ∼10 au where the previous study showed that the spectral index between Bands 4 and 6 is lower than 2 (Tsukagoshi et al. 2016). In order to investigate each data with the same beam size, the observed images at Bands 4, 6, 7, and 9 are re-convolved with the beam size of Band 3 observation (0.43 × 0.″27), which is equivalent to the spatial resolution of 26 × 16 au for the distance of the target from the Earth (≈60 pc, Gaia Collaboration et al. 2016).

The intensities at the center of the re-convolved images at each band are shown in Figure 2 and summarized in Table 1. Since the spatial resolution of 26 × 16 au corresponds to the effective beam radius of 10 au, the intensity at the center of the images traces mainly the inner disk within the radius of ∼10 au. In Figure 2, we plot error bars corresponding to 5% of the absolute intensity for Bands 3 and 4, 10% for Bands 6 and 7, and 20% for Band 9. The errors are potentially caused in the flux calibration process and quoted from the ALMA official observing guide. In the Appendix, we examined the time variation of the flux density of the amplitude calibrators to see

Table 1
Observed Intensity at the Center of the Images and the 1σ Noise Level at Different Observing Wavelengths

Wavelength (μm)	Intensity (mJy/beam)	Noise (mJy/beam)	Uncertainty (mJy/beam)
453.5 (B9)	499	1.1	±99.8
921.3 (B7)	122	0.24	±12.2
1287 (B6)	76.7	0.12	±7.67
2068 (B4)	31.0	0.091	±1.55
3064 (B3)	15.1	0.025	±0.755

Note. The uncertainty in the absolute intensity is set to be 5% for Bands 3 and 4, 10% for Bands 6 and 7, and 20% for Band 9.

the actual uncertainty. We confirmed that the actual uncertainty might be potentially larger than the official value but has little impact on our conclusion.

Figure 2 shows that the observed SED does not follow a single power-law profile. The spectral slope through Bands 3 to 6 can be explained by the spectral index of 2 within the error. The spectral index lower than 2 between Bands 4 and 6 reported by Tsukagoshi et al. (2016) is also consistent with our analysis. In contrast, the intensities at Bands 7 and 9 are lower than the intensity extrapolated from longer wavelengths with spectral slopes of 2. The spectral index between Bands 6 and 7 is ≈1.4, which is significantly lower than 2. The anomalously low spectral index around Band 7 is consistent with previous studies within the error (Nomura et al. 2016; Huang et al. 2018a). In addition, the spectral index between Bands 6 and 9 is ≈1.6, which is also lower than 2 but higher than that between Bands 6 and 7.

The observed low spectral indices through Bands 6 to 9 indicate that the scattering-induced intensity reduction occurs, and it is the most effective at Band 7 in the inner region of the disk. To explain the observed SED of the inner part of the TW Hya disk, we perform radiative transfer simulations in the following section.

3. Radiative Transfer Modeling

3.1. Modeling Concepts

In this subsection, we briefly describe the concept of how we model the simulated disks.

As a first step, we compare the blackbody curves with different temperatures $T_{\rm BB}$ to the observed SED in Figure 3. Figure 3 shows that the observed SED is similar to the blackbody curve with a temperature of ∼23 K. Because the disk is likely optically thick at Band 9 and the observed intensity at Band 9 can be reproduced with $T_{\rm BB} \gtrsim 23$ K, the lower limit of the disk temperature can be estimated as ∼23 K. If the scattering-induced intensity reduction occurs at Band 9, the disk temperature could be higher than 23 K.

The observed intensity at Band 3 is almost consistent with the blackbody curve with $T_{\rm BB} = 23$ K or slightly lower. Therefore, if scattering is not effective at Band 3 and the temperature is 23 K, the disk is (marginally) optically thick even at Band 3. If the temperature is higher than 23 K, the disk should be optically thin or scattering should be effective.

In this work, we focus only on the emission from the center of the disk images, which is observed with a beam radius of ∼10 au. Since the emission would be dominated by the outer part within the observing beam, these estimated temperatures and optical thicknesses would trace values at the outer edge of the beam (∼10 au from the center). From these analyses, we model the disk so that the disk is marginally optically thin/thick at Band 3, and the temperature is higher than 20 K at 10 au. A detailed setup will be shown in the following section.

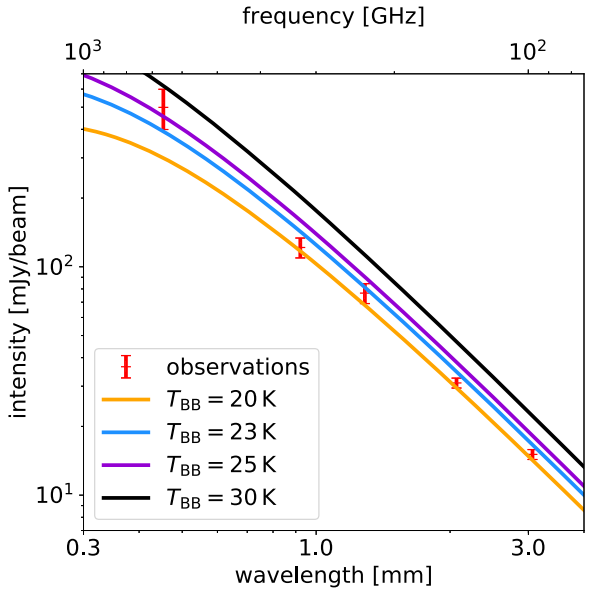

Figure 3. Blackbody curves at dust temperatures of 20 K (orange), 23 K (light blue), 25 K (purple), and 30 K (black). The red points show the intensities at the center of the observed images.

3.2. Radiative Transfer Setup

In order to investigate the properties of the inner part of the TW Hya disk, radiative transfer simulations are performed with the Monte Carlo radiative transfer code RADMC-3D (Dullemond et al. 2012). For dust opacities, we use the DSHARP dust optical constants published in Birnstiel et al. (2018; see also Henning & Stognienko 1996; Draine 2003; Warren & Brandt 2008 for the optical constants of each dust component). The dust grains are assumed to be spherical compact grains with a material density of 1.675 g cm^{-3}. The dust size distribution is assumed to be a power-law distribution ranging from 0.1 μm to $a_{\rm max}$ with a power-law index of 3.5. To treat full anisotropic scattering, the Müeller matrices are calculated using the Mie theory, specifically the Bohren-Huffman program (Bohren & Huffman 1983). Figure 4 shows the effective scattering albedo $\omega_{\rm eff}$ for the different maximum dust sizes. The effective scattering albedo is defined as

$$\omega_{\rm eff} = \frac{\kappa_{\rm sca}^{\rm eff}}{\kappa_{\rm abs} + \kappa_{\rm sca}^{\rm eff}}, \quad (1)$$

where $\kappa_{\rm abs}$ is the absorption opacity and $\kappa_{\rm sca}^{\rm eff}$ is the scattering opacity considering the effect of forward scattering. The values of the effective scattering albedo at each observing band are summarized in Table 2. At (sub)millimeter wavelengths, the effective scattering albedo increases with the wavelength when the wavelength is shorter than $\sim 2\pi a_{\rm max}$ and has a maximum at around $\lambda \sim 2\pi a_{\rm max}$ and drops off when $\lambda > 2\pi a_{\rm max}$.

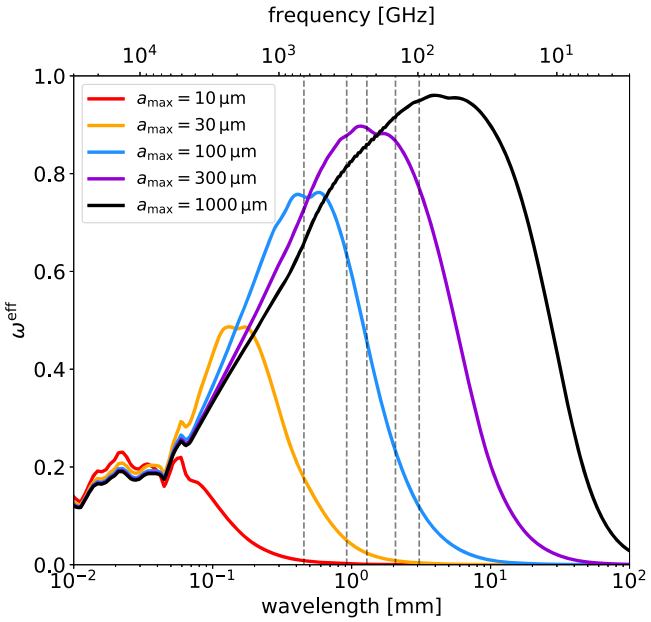

Figure 4. Effective scattering albedo $\omega_{\rm eff}$ as a function of the wavelength for the different maximum dust sizes. The gray vertical dashed lines show the observing wavelengths at Bands 3, 4, 6, 7, and 9 from right to left.

Table 2
Effective Scattering Albedo $\omega_{\rm eff}$ at Each Observing Band

$a_{\rm max}$\Band	3	4	6	7	9
10 μm	0.00015	0.00033	0.00094	0.0020	0.0085
30 μm	0.0037	0.0084	0.024	0.050	0.18
100 μm	0.12	0.23	0.46	0.63	0.75
300 μm	0.77	0.87	0.89	0.88	0.73
1000 μm	0.95	0.92	0.86	0.82	0.66

In our simulations, the dust surface density is assumed to follow a simple power-law profile:

$$\Sigma_{\rm d} = \Sigma_{10}\left(\frac{r}{10\ {\rm au}}\right)^{-0.5}, \quad (2)$$

where r is the mid-plane distance from the central star and Σ_{10} is the dust surface density at 10 au. The inner edge of the disk is set to 1 au to mimic the presence of an inner cavity in the TW Hya disk. We truncate the disk at 50 au, which is far enough from the center of the disk as to not affect the intensity at the center when the intensity is convolved with the observing beam size ($\sim$20 au). The dust surface density is related to the vertical absorption optical depth at Band 3 at 10 au as

$$\tau_{10} = \kappa_{\rm B3}\Sigma_{10}, \quad (3)$$

where $\kappa_{\rm B3}$ is the absorption opacity at the observing frequency of Band 3. Using the dust surface density, the dust volume density $\rho_{\rm d}$ is calculated as

$$\rho_{\rm d} = \frac{\Sigma_{\rm d}}{\sqrt{2\pi}\,h_{\rm d}}\exp\left(-\frac{z^2}{2h_{\rm d}^2}\right), \quad (4)$$

where z is the vertical height from the mid-plane and $h_{\rm d}$ is the scale height of the dust disk,

$$h_{\rm d} = 0.63\left(\frac{r}{10\ {\rm au}}\right)^{1.1}\ {\rm au}. \quad (5)$$

The temperature profile is assumed to be

$$T(r,\,\phi,\,z) = T_{10}\left(\frac{r}{10\ {\rm au}}\right)^{-0.4}, \quad (6)$$

where ϕ is the azimuthal angle and T_{10} is the temperature at 10 au. The disk inclination is set to be 7° based on Qi et al. (2004). The simulated images are convolved with the observing beam size.

In the following subsections, we show the comparison between the ALMA observations and the results of the radiative transfer simulations with and without scattering.

3.3. Step 1—No-scattering Case

As shown in Figure 2, the intensities at short wavelengths are lower than the intensity extrapolated from longer wavelengths with the spectral slope of 2. At short wavelengths, the observing wavelength would be close to the peak wavelength of the blackbody emission from the disk so that the blackbody emission might be deviated from and lower than the Rayleigh–Jeans limit (e.g., Figure 5 of Kim et al. 2019).

In order to investigate whether the observed low intensity at high frequency can be explained simply by the deviation from the Rayleigh–Jeans limit, we first show the results of radiative transfer simulations without scattering in Figure 5. In Figure 5, we change the disk temperature, and the disk mass (i.e., τ_{10}) is set for each temperature model so that the observed intensity at Band 3 is reproduced. If $T_{10} = 20$ K, the simulated intensity profile is similar to the observed one between Bands 3 and 7 but is significantly lower at Band 9. If T_{10} is higher than 30 K, the model overpredicts the intensity at Bands 4–9. Although the observed intensity profile is barely reproduced by the model with $T_{10} = 22$ K, the model intensities are the lower limit of the Band 9 observation and are higher at Band 6. If T_{10} is higher than 22 K, the intensity at an observing wavelength shorter than Band 4, especially at Bands 4, 6, and 7, is significantly higher than the observed value. Since the disk is optically thick at $\lambda \lesssim 3$ mm in all of these models, the impact of dust size arises only at $\lambda \gtrsim 3$ mm. Therefore, we conclude that, if scattering is not taken into account, it is difficult to explain the observed intensity profile except for the model with $\tau_{10} = 2.2$ and $T_{10} = 22$ K.

3.4. Step 2—Turning on the Scattering Effect

As the observed SED suggests that dust scattering is the most effective at Band 7, we first perform the radiative transfer simulation with turning on scattering, and we set the maximum dust radius to be 300 μm, whose albedo has a peak around Bands 6–7 (see Figure 4).

Figure 6 shows the comparison between the observed intensity and the simulated intensity of the model with a maximum dust radius of 300 μm with and without scattering. In Figure 6, τ_{10} and T_{10} are set to be 0.95 and 30 K, respectively. We clearly see that the model with scattering well produces the observed intensities while the model without scattering overestimates. As the scattering albedo of 300 μm

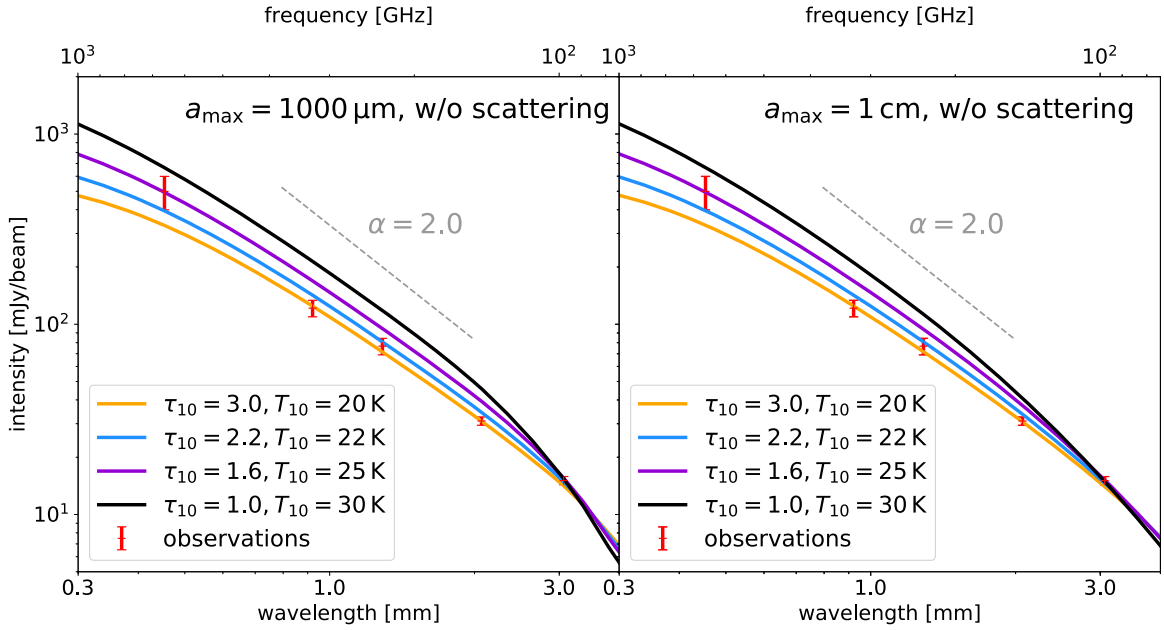

Figure 5. Intensity at the center of the disk images simulated without scattering. The orange, light blue, purple, and black solid lines show the simulated intensity for the different disk models. The maximum dust size is set to be 1000 μm and 1 cm in the left and right panels, respectively. The red points show the observed values. The gray dashed line denotes a spectral index of 2.

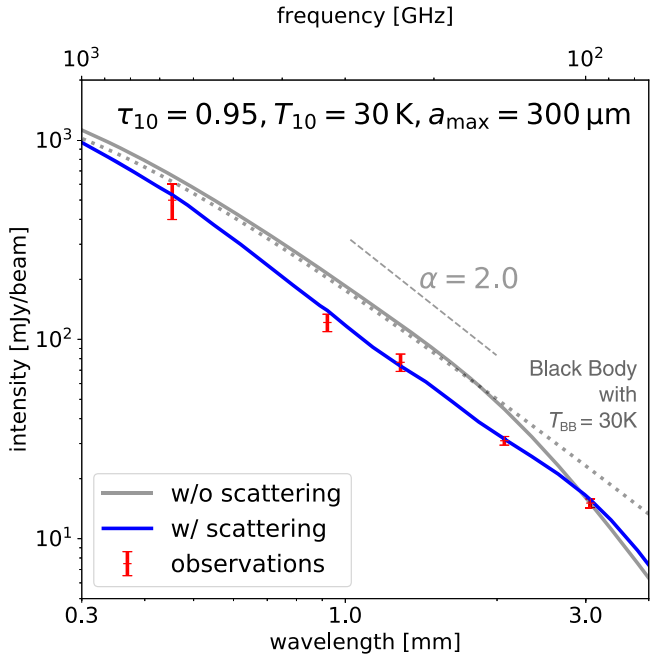

Figure 6. Intensity at the center of the disk images. The blue and gray solid lines show the simulated intensity for the maximum dust size of 300 μm with and without scattering, respectively. The vertical absorption optical depth at 10 au is set to be 0.95 at Band 3, and the temperature at 10 au is set to be 30 K. The red points show the observed values. The gray dotted line shows the blackbody curve at a dust temperature of 30 K. The gray dashed line denotes a spectral index of 2.

grains has a peak around Bands 6–7, scattering is the most effective at Bands 6–7 and reduces the intensity at those bands by ∼35%.

On the other hand, at wavelengths longer than 3 mm, the model with scattering shows a slightly higher intensity than the model without scattering. This would be because, if the observed region is optically thin for the vertical direction but optically thick for the radial direction, scattered photons selectively escape to the vertical direction, which enhances the disk brightness compared to the no-scattering case. In this model, dust scattering enhances the observed intensity by ∼20% at the maximum compared to the model without scattering. This intensity enhancement by scattering can be also seen in Figure 9 of Birnstiel et al. (2018), although they have not mentioned it.

3.5. Step 3—Fine-tuning of Grain Size

From the observed SED, one would expect that dust scattering reduces the observed intensity only in observing wavelengths shorter than 1 mm. This implies that dust grains need to be smaller than 1 mm, otherwise dust scattering is effective even at longer observing wavelengths. In order to investigate the dependence of the SED on the dust size, we perform radiative transfer simulations with different dust sizes.

Figure 7 shows simulated intensities with different dust sizes for the same disk temperature and mass with the model shown in Section 3.4. If the maximum dust radius is 10 μm, scattering is not effective, so the simulated intensity is almost the same as that of the no-scattering model shown in Figure 6. For the 100 μm grains, the effect of scattering shows up and is more effective in shorter observing wavelengths since the scattering albedo of 100 μm grains monotonically decreases with the wavelength within the observing wavelengths. These results indicate that dust grains smaller than 100 μm do not account for the observed intensity profile, which has a dip around Band 7. In contrast, if the dust size is larger than 1000 μm, scattering is the most effective at Band 3 since the scattering albedo monotonically increases with wavelength, which leads to an underestimate of the intensity at Band 3. Therefore, the maximum dust radius of ∼300 μm, whose scattering albedo has a peak around Bands 6–7, is the best to explain the observed intensity profile.

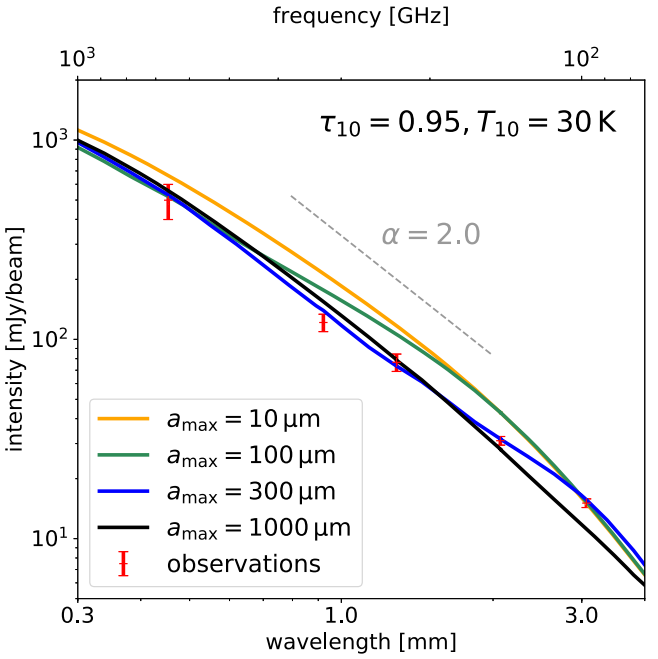

Figure 7. Intensity at the center of the disk images. The orange, green, blue, and black solid lines show the simulated intensities for a maximum dust size of $a_{max} = 10$, 100, 300, and 1000 μm, respectively. The vertical optical depth at 10 au is set to be 0.95 at Band 3, and the temperature at 10 au is set to be 30 K. The red points show the observed values. The gray dashed line denotes a spectral index of 2.

3.6. Modeling Summary

In this subsection, we briefly summarize our findings of the disk modeling. First, if scattering is not taken into account, it is difficult to reproduce the observed SED except for the model with $\tau_{10} = 2.2$ and $T_{10} = 22$ K. The models with $T_{10} > 22$ K overpredict the intensity at Bands 4–7, while the model with $T_{10} < 22$ K underestimates the intensity at Band 9. If dust scattering is taken into account, the model with a maximum dust radius of 300 μm well reproduces the observed SED. Since dust scattering reduces the intensity by ~35% at Band 7, the disk needs a higher temperature ($T_{10} = 30$ K) than the model without scattering ($T_{10} = 22$ K). The optical depth is determined to be $\tau_{10} = 0.95$ since the disk is marginally optically thin at Band 3.

The schematic of protoplanetary disks with scattering is illustrated in Figure 8. If the disk is optically thick for self-scattering in both the vertical and radial directions, the thickness of the disk layer where we can see is reduced by scattering because the mean free path of the emitted photons ℓ_{eff} is $(\rho_d \sqrt{\kappa_{abs}(\kappa_{abs} + \kappa_{sca}^{eff})})^{-1}$, which is shorter than that without scattering by a factor of $\sqrt{1 - \omega_{eff}}$ (e.g., Rybicki & Lightman 1979). If the disk is optically thin for self-scattering in the vertical direction but thick in the radial direction, the intensity is enhanced by scattering because the scattered photons selectively escape to the disk surface. The best-fit model in this paper suggests that, at long observing wavelengths (>3 mm), the intensity is higher than that expected from the model without scattering by 20% at the maximum (at $\lambda \sim 4$ mm). In the region where the disk is optically thin for self-scattering in both the vertical and radial directions, scattering can be ignored.

4. Discussion

4.1. Dependence on the Opacity Model

Our results showed that the TW Hya disk needs to have a vertical absorption optical depth of 0.95 at 10 au at Band 3. The DSHARP opacity we use has an absorption opacity of 9.2×10^{-2} cm^2 g^{-1} at the wavelength of Band 3 ($\lambda = 3.1$ mm), meaning that the dust surface density needs to be 10 g cm^{-2} at 10 au. This is 19 times higher than the MMSN model (Hayashi 1981).

The absolute value of the absorption opacity strongly depends on dust properties, such as composition and porosity, and has a large uncertainty (e.g., Draine 2006; Kataoka et al. 2014; Min et al. 2016; Woitke et al. 2016; Birnstiel et al. 2018; Tazaki & Tanaka 2018). Especially if dust grains contain carbonaceous materials such as graphite (Draine 2003) and cosmic carbon analogs (Zubko et al. 1996), the absorption opacity can be higher than the DSHARP opacity by an order of magnitude at millimeter wavelengths, which would lead to a surface density lower than we expect by an order of magnitude.

However, if dust grains contain cosmic carbon analogs, the scattering albedo at a wavelength of ~1 mm is as high as 0.6 and has a flat profile as a function of the wavelength, as shown in Figure 9. This indicates that the cosmic carbon dust might not account for the observed intensity profile of the inner region of the TW Hya disk, which has a dip at Band 7.

4.2. Fragmentation of Dust Particles

Our results showed that the inner region of the TW Hya disk is dominated by ~300 μm-sized grains. The small size of the dust grains indicates that dust fragmentation is effective in the inner region of the disk. Here, let us estimate for which conditions the estimated dust size can be explained by dust fragmentation. If dust size is regulated by turbulence-induced collisional fragmentation, the maximum dust size is estimated as (e.g., Birnstiel et al. 2009; Okuzumi & Tazaki 2019; Ueda et al. 2019)

$$a_{max} = \frac{2}{3\pi} \frac{\Sigma_g}{\alpha_{turb} \rho_d} \left(\frac{v_{frag}}{c_s} \right)^2, \quad (7)$$

where α_{turb} is the turbulence strength, Σ_g is the gas surface density, ρ_d is the material density of the dust grain, v_{frag} is the fragmentation velocity of the dust grains, and c_s is the sound speed of the gas. Therefore, the turbulence strength is estimated as a function of the maximum dust size as

$$\alpha_{turb} = 6.6 \times 10^{-2} \left(\frac{a_{max}}{300\ \mu\text{m}} \right)^{-1} \left(\frac{\Sigma_g}{20\ \text{g cm}^{-2}} \right) \times \left(\frac{v_{frag}}{10\ \text{m s}^{-1}} \right)^2; \quad (8)$$

here, we assume $\rho_d = 1.675$ g cm^{-3} and $T = 30$ K. The critical fragmentation velocity for water-ice grains is estimated as ~8–80 m s^{-1} (e.g., Wada et al. 2013; Gundlach & Blum 2015). Therefore, although the gas surface density of the TW Hya disk is uncertain as discussed in Section 4.3, Equation (8) indicates that the disk needs to be highly turbulent ($\alpha_{turb} \gtrsim 10^{-2}$) and/or the dust grains need to be less sticky than the water ice; otherwise, the gas surface density will be lower than the dust

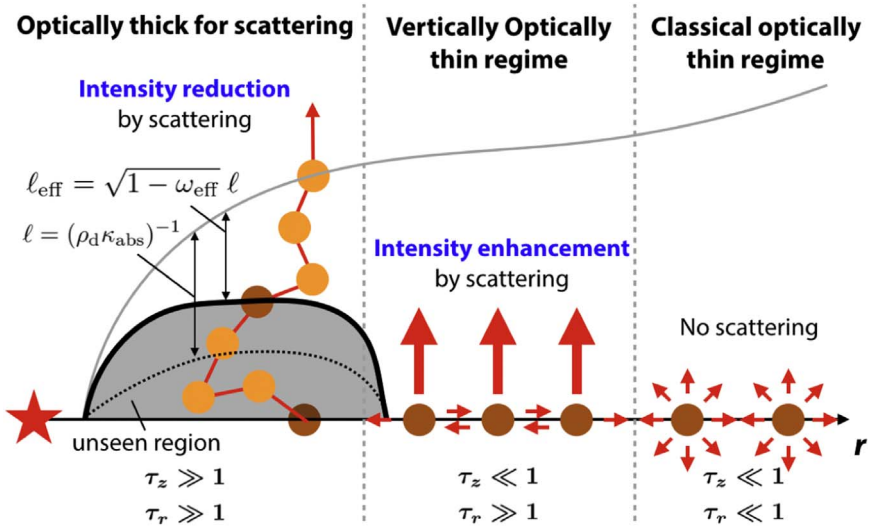

Figure 8. Schematic of protoplanetary disks with dust scattering. In the inner region of the disk, the disk is optically thick in both the vertical and radial directions so that we can only see the surface layer with a depth of $\ell_{\rm eff} = \sqrt{1-\omega_{\rm eff}}\,\ell$, where ℓ is the mean free path of the emitted photons in the limit of no-scattering. In the intermediate region, the disk becomes optically thin in the vertical direction so that the scattered photons selectively escape to the vertical direction, which enhances the disk brightness. In the outer region, the disk is optically thin in both the vertical and radial directions so that scattering can be ignored.

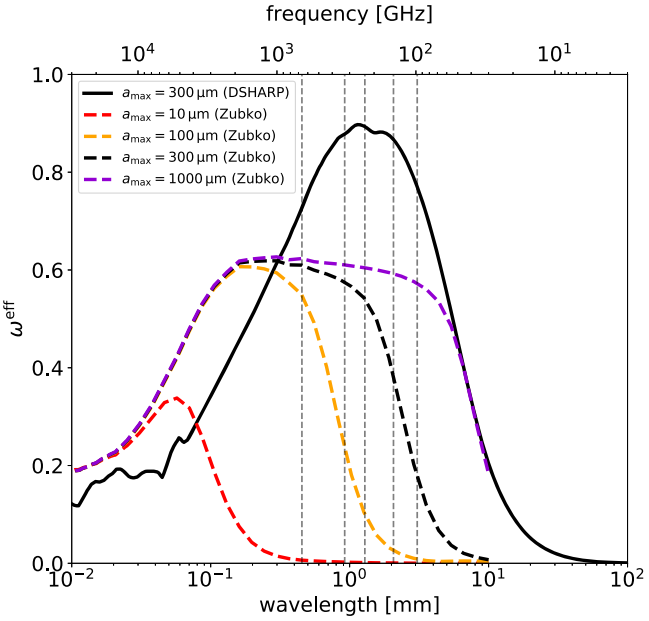

Figure 9. Effective scattering albedo $\omega_{\rm eff}$ of cosmic carbon dust (Zubko et al. 1996). The red, orange, black, and purple dashed lines show $\omega_{\rm eff}$ of the cosmic carbon dust with maximum dust sizes of 10, 100, 300, and 1000 μm, respectively. The black solid line denotes the DHARP dust with a maximum dust size of 300 μm.

surface density. The poor stickiness of icy grains might be explained by dust grains that are covered by a CO_2 mantle, which is less sticky than water ice (Musiolik et al. 2016; Okuzumi & Tazaki 2019).

The turbulence strength in the TW Hya disk has been measured from the turbulent broadening of molecular emission lines and found to be ~0.001 at most (e.g., Flaherty et al. 2018; Teague et al. 2018). Although these observations trace the turbulence strength at the surface layer of the outer region of the disk, this relatively weak turbulence indicates that the sticking efficiency of dust grains is considerably low in the inner region of the TW Hya disk.

4.3. Disk Masses

Our results showed that the dust surface density needs to be ~10 g cm^{-2} at 10 au if scattering is taken into account. Since the spatial resolution of our data set is not high enough, it is hard to discuss the detailed radial profile of the dust surface density. However, it would be worth it to estimate the potential dust mass residing in the inner region of the TW Hya disk. If we assume a dust column density profile of 10 g cm^{-2} at 10 au with a slope of −0.5, the inner region (<10 au) of the TW Hya disk has a total dust mass of 150 $M_\oplus$, which is enough to form cores of giant planets. Previous studies have shown that the total dust mass in the whole disk is around 150 $M_\oplus$ (Calvet et al. 2002; Thi et al. 2010), which is comparable to the mass residing within 10 au. This implies that, even though the total dust mass has been thought to be dominated by the outer region because of its large surface area, the TW Hya disk has a significant amount of dust within the optically thick inner region and is still capable of forming the cores of giant planets at locations analogous to where the current solar system planets exist. This might solve the problem that the observed dust masses in the disks are significantly lower than the solid mass in observed exoplanets (Manara et al. 2018).

If the dust-to-gas mass ratio has a fiducial value of 0.01, the gas surface density is 1000 g cm^{-2} at 10 au. However, the high gas surface density might make the disk unstable. Here, let us estimate the criterion of the dust-to-gas mass ratio to avoid gravitational instability. The gravitational stability of a disk can be evaluated by Toomre's Q parameter (Toomre 1964):

$$Q \equiv \frac{c_{\rm s}\Omega_{\rm K}}{\pi G \Sigma_{\rm g}}, \tag{9}$$

where G is the gravitational constant. If Q is lower than ~1, the disk is gravitationally unstable. Assuming $T = 30$ K and a stellar mass of 0.8 $M_\odot$, the condition for the disk to be gravitationally stable at 10 au is estimated as

$$\Sigma_{\rm g,10\,au} < 874\ {\rm g\ cm^{-2}}. \tag{10}$$

Therefore, the disk is marginally unstable for self-gravity at 10 au if the dust-to-gas mass ratio is 0.01.

The mass of the gas disk in the inner part of the TW Hya disk is still uncertain. The gas surface density of the inner part of the TW Hya disk has been estimated by using observations of the $^{13}C^{18}O$ $J = 3 - 2$ line emission and found to be $13^{+8}_{-5} \times (r/20.5\,\mathrm{au})^{-0.9^{+0.4}_{-0.3}}\,\mathrm{g\,cm^{-2}}$ (Zhang et al. 2017). If the dust surface density is 10 g cm^{-2} at 10 au, the dust-to-gas mass ratio is 0.4 at 10 au, which would be high enough to trigger planetesimal formation via streaming instability (e.g., Youdin & Goodman 2005; Carrera et al. 2015; Yang et al. 2017).

It would be worth being notified that the gas mass estimated by Zhang et al. (2017) is based on the dust distribution derived by Hogerheijde et al. (2016, and also Andrews et al. 2016). Hogerheijde et al. (2016) have estimated the dust surface density at 10 au to be 0.39 g cm^{-2}, assuming an absorption opacity at Band 7 of 3.4 cm^2 g^{-1}, which leads to an optical depth of 1.3 at 10 au at Band 7. In contrast, our results showed that the dust surface density would be ∼26 times higher than that estimated by Hogerheijde et al. (2016). This difference comes from the assumption of no-scattering in Hogerheijde et al. (2016). Our results also showed that scattering reduces the intensity by ∼35% at Band 7. Interestingly, if one tries to fit the reduced intensity (i.e., $0.65B_\nu(T = 30\,\mathrm{K})$) assuming no-scattering, one can obtain an optical depth of 1.3 for a temperature of 26.7 K, which is consistent with the results of Hogerheijde et al. (2016; i.e., $0.65B_\nu(T = 30\,\mathrm{K}) \approx (1 - \exp(-1.3))B_\nu(T = 26.7\,\mathrm{K})$). Therefore, previous estimates assuming no-scattering have led to an underestimation of the dust mass by a factor of 26. If the dust density is higher than that previously predicted, the gas surface density might also be higher than that expected by Zhang et al. (2017) since the line emission is hidden in the optically thick region.

4.4. Scattered Light Observations

The inner region of the TW Hya disk is bright in (sub) millimeter wavelengths but dark in infrared wavelengths (van Boekel et al. 2017). Our results showed that the maximum dust size is ∼300 μm in the inner region of the TW Hya, implying that dust fragmentation efficiently supplies small grains that contribute to scattering of the stellar light at the disk surface, which is intuitively inconsistent with scattered light observations.

A simple explanation for this discrepancy is that the dust size distribution is no longer a simple power-law distribution, and small grains are less numerous than we expect, but we would like to refer to two hypotheses that potentially explain this discrepancy. One solution is a shadow casted by the inner rim of the dust disk or the dust concentration at the inner-most region of the disk (e.g., Dullemond et al. 2001; Dullemond & Monnier 2010; Ueda et al. 2019). These structures block the stellar light, and the shaded region just behind them becomes dark in the scattered light images even if the disk has a lot of small grains. Since these effects strongly depend on the shape of the disk surface at the inner-most region of the disk (e.g., Menu et al. 2014), detailed modeling and high angular resolution observations are necessary to comprehensively understand the multiwavelength images.

The other solution is the ineffective vertical mixing of dust grains. If the dust-to-gas mass ratio is high, the disk gas no longer lifts dust grains to the upper layer due to the back-reaction from dust to gas (e.g., Lin 2019). The resultant low disk surface would make the disk fainter in the scattered light images. However, in this situation, fragmentation of the dust grains might be also ineffective since it is difficult for the disk gas to affect the dust motion.

4.5. Prevalence of 100 μm-sized Grains

Our results showed that the maximum dust size is ∼300 μm in the inner region of the TW Hya disk. Recently, in some disks, ALMA polarimetric observations have successfully detected scattering-induced polarization where the polarization vector is parallel to the minor axis of the disk (e.g., Stephens et al. 2017; Bacciotti et al. 2018; Hull et al. 2018; Dent et al. 2019). Interestingly, many of these disks have shown a scattering-induced polarization pattern in the entire region of the disks at a wavelength of ∼1 mm, indicating that the maximum dust size is of the order of 100 μm in these disks. These polarimetric observations suggest that 100 μm-sized grains are prevalent even in different disks and different regions of the disk. However, theoretically, it is not easy for dust grains to maintain a size of 100 μm. If the dust size is regulated by the collisional fragmentation, the maximum dust size would be a function of the gas surface density (Equation (7)) since the kinematic motion of grains is determined by the fluid motion. Therefore, if the maximum dust size is uniformly 100 μm in the disk and even in the other disks, the gas surface density also needs to be uniform (Okuzumi & Tazaki 2019), which is not very intuitive. We may need a universal way for dust grains to maintain a size of ∼100 μm for different disk conditions.

4.6. Solving a Degeneracy between Models with and without Scattering

Although the model with scattering well reproduces the observed millimeter SED, the model without scattering is also consistent with the observations within the errors in the absolute intensities. Due to the errors, it is not easy to solve the degeneracy between these models. One possible solution to the degeneracy is measuring the intensity at shorter wavelengths, e.g., at ALMA Band 10 ($\lambda \sim 0.35$ mm). Figure 10 shows the millimeter SED of the best models in simulations with and without scattering. For the model without scattering, the SED depends on the dust radius at wavelengths longer than ∼3 mm, since the disk is optically thin. Because the model with scattering needs a higher temperature than the model without scattering, and the scattering effect gets weaker at shorter wavelengths, the model with scattering predicts a higher intensity at wavelengths shorter than ∼0.5 mm. Our results suggest that at the center part of the TW Hya disk, the intensity is ∼40% higher in the model with scattering at ALMA Band 10. Observations at longer wavelengths also might potentially solve the degeneracy, but the model without scattering might produce the same results as the model with scattering, since the intensity depends on the dust radius.

5. Summary

We investigated the inner part of the TW Hya disk by analyzing ALMA observations at Bands 3, 4, 6, 7, and 9, and we compared our analysis to models obtained from radiative transfer simulations with and without scattering. The ALMA multiband analysis showed that, in the inner region of the disk ($\lesssim$10 au), the observed intensities at Bands 7 and 9 are lower

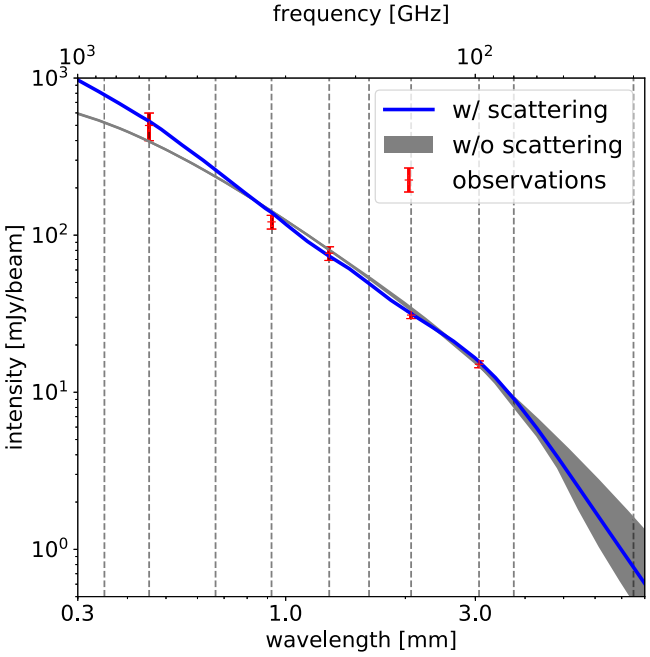

Figure 10. Millimeter SED of the best models in simulations with and without scattering. The blue solid line shows the model with a maximum dust radius of 300 μm that includes scattering. For the simulation with scattering, the vertical absorption depth is set as $\tau_{10} = 0.95$ and the temperature is set as $T_{10} = 30$ K. The gray area corresponds to the intensity simulated without scattering. For the simulations without scattering, we set $\tau_{10} = 2.2$ and $T_{10} = 22$ K and change the dust radius from 10 μm to 10 cm. The vertical dashed lines show the ALMA observing wavelengths at Bands 1 to 10 from right to left.

than the intensity extrapolated from longer wavelengths with a spectral slope of 2. The intensity profile through Bands 3 to 6 can be explained by a spectral index of 2 within the errors. Although the intensity at shorter wavelengths has a large uncertainty, the spectral index is estimated as ∼1.4 between Bands 6 and 7 and ∼1.6 between Bands 6 and 9.

To investigate the properties of the inner region of the TW Hya disk, radiative transfer simulations were performed with the Monte Carlo radiative transfer code RADMC-3D. We found that the model with scattering well reproduces the observations, but the model without scattering is also consistent with the observations within the errors in the absolute flux densities. From the intensity at Band 3, the optical depth at 10 au at Band 3 is estimated as 0.95 and 2.2 for the models with scattering and without scattering, respectively. In the model with scattering, the observed millimeter SED can be reproduced by the model with a maximum dust radius of ∼300 μm. For the opacity model we used, the dust surface density needs to be 10 g cm^{-2} at 10 au, which is 26 times higher than previously predicted. This large discrepancy comes from the intensity reduction by dust scattering, which makes the disk look optically thin even if it is sufficiently optically thick. The small maximum grain size indicates that dust fragmentation is effective in the inner part of the TW Hya disk. If the critical fragmentation velocity of dust grains is 10 m s^{-1}, the turbulence strength needs to be higher than $\sim 10^{-2}$; otherwise, the gas surface density is lower than the dust surface density. The high dust surface density might trigger planetesimal formation via streaming instability in the inner region of the TW Hya disk.

We would like to thank the anonymous referees for useful comments that significantly improved our study. We would like to thank Satoshi Okuzumi for useful comments. This paper makes use of the following ALMA data: ADS/JAO.ALMA#2012.1.00422.S, ADS/JAO.ALMA#2013.1.00114.S, ADS/JAO.ALMA#2015.A.00005.S, ADS/JAO.ALMA#2015.1.00308.S, ADS/JAO.ALMA#2015.1.00686.S, ADS/JAO.ALMA#2016.1.00229.S, ADS/JAO.ALMA#2016.1.00311.S, ADS/JAO.ALMA#2016.1.00440.S, ADS/JAO.ALMA#2016.1.00464.S, ADS/JAO.ALMA#2016.1.00629.S and ADS/JAO.ALMA#2016.1.01495.S. ALMA is a partnership of ESO (representing its member states), NSF (USA) and NINS (Japan), together with NRC (Canada) and NSC and ASIAA (Taiwan) and KASI (Republic of Korea), in cooperation with the Republic of Chile. The Joint ALMA Observatory is operated by ESO, AUI/NRAO, and NAOJ. This work was supported by JSPS KAKENHI grant No. JP19J01929.

Software: RADMC-3D (Dullemond et al. 2012).

Appendix
Time Variability of Calibrator Fluxes

In this section, we show the time variability of flux densities of the amplitude calibrators and discuss the uncertainty in the absolute flux density of the target source. The flux densities of the calibrators were taken from the ALMA Calibrator Source Catalogue (https://almascience.eso.org/sc/).

In the calibration process, the flux density of the target is scaled with respect to that of the amplitude calibrator. The flux density of the calibrator is determined by observing solar system objects near the observing date. Since the flux density of the calibrator is time-variable, the time difference between the observing day of the target and the calibrator would cause an uncertainty in the absolute flux density.

Table A1 lists the ALMA project IDs used in this study and the amplitude calibrators used in the calibration process. We analyzed a single data set for Band 3, 4, and 9 data, whereas some execution blocks were concatenated for Bands 6 and 7.

For the calibration of Band 3, 4, and 6 observations, quasar J1037–2934 is used as the amplitude calibrator. Figure A1 shows the time dependence of the observed flux density of J1037–2934 at Band 3 before and after the day when TW Hya was observed. We clearly see that the flux density decreases across the day when TW Hya was observed. To estimate the actual flux density of the calibrator on the day when TW Hya was observed, we fit the observed flux densities with a linear function. The standard errors (σ) of the observed flux density around the fitting formula at $\nu = 91.5$ and 103 GHz are 4.4% and 3.9%, respectively. However, the adopted flux density is higher than the value estimated from the fitting by ∼5%–10%, which is larger than the standard error.

One of the causes of the discrepancy is that the adopted calibrator flux density is determined using the data before the calibration has been done, which means that long-term variation across the observing day might not be correctly taken into account. To reduce the uncertainty caused by long-term variation, it is necessary to determine the calibrator flux density using the data before and after the observing day of the target. In addition to long-term variation, the flux density of the calibrator might change with short timescales, which are hard to be quantified with the given observing interval. To reduce the uncertainty caused by short-term variation, we should

Table A1
ALMA Observations Used in This Study and Its Flux Calibrators

Band	Project ID	Number of Execution Blocks	Amplitude Calibrator	Adopted Flux Density (Jy)	Spectral Index	at GHz
3	2016.1.00229.S	1	J1037−2934	1.46	−0.647	97.8
4	2015.A.00005.S	1	J1037−2934	0.948	−0.468	145
6	2013.1.00114.S	1	J1037−2934, (Pallas)			
	2015.A.00005.S	1	J1037−2934	0.759	−0.468	233
7	2015.1.00308.S	2	J1037−2934	0.585	−0.638	315
			J1107−4449	0.655	−0.721	
	2015.1.00686.S	3	J1037−2934	0.604	−0.492	351
			J1107−4449	0.542	−0.711	
			J1037−2934	0.627	−0.468	
	2016.1.00229.S	1	J1107−4449	0.407	−0.811	337
	2016.1.00311.S	1	J1037−2934	1.19	−0.520	340
	2016.1.00440.S	1	J1107−4449	0.430	−0.823	349
	2016.1.00464.S	7	J1037−2934	0.685	−0.481	303
			J1037−2934	0.685	−0.481	
			J1037−2934	0.679	−0.481	
			J1037−2934	0.679	−0.481	
			J1037−2934	0.679	−0.481	
			J1037−2934	0.679	−0.481	
			J1037−2934	0.679	−0.481	
	2016.1.00629.S	2	J1037−2934	0.788	−0.357	344
			J1037−2934	0.788	−0.357	
	2016.1.01495.S	2	J1037−2934	0.652	−0.488	331
			J1037−2934	0.652	−0.481	
9	2012.1.00422.S	1	J1037−2934, (Titan)			

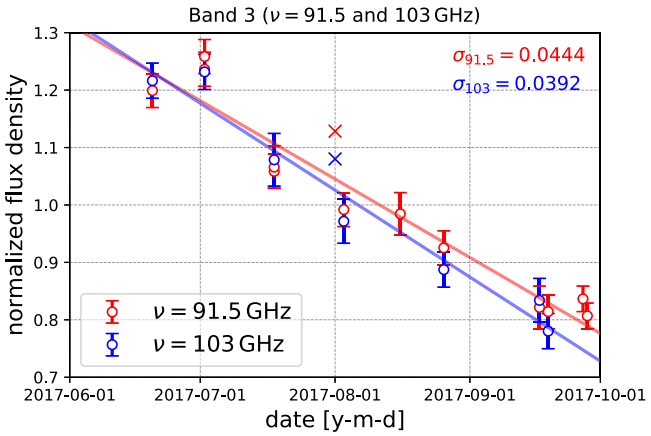

Figure A1. Time dependence of the flux density of J1037–2934 at Band 3. The red and blue circles show the flux density at $\nu = 91.5$ and 103 GHz, respectively. The red and blue solid lines denote the linear fitting of the observed flux densities at $\nu = 91.5$ and 103 GHz, respectively. The crosses correspond to the flux density estimated from the flux density and spectral index adopted in the calibration process. The flux is normalized by the average.

determine the flux density of the amplitude calibrator at the same time of the target observation.

The Band 4 observations also employed J1037−2934, but the flux density at Band 4 was not monitored around the observation date. According to the calibration script that ALMA provided, the adopted flux density of the calibrator at Band 4 is 0.948 Jy at a reference frequency of 145 GHz with a spectral index of −0.468. Figure A2 compares the observed flux density of J1037–2934 at Bands 3, 6, and 7 with the flux densities at those bands estimated from the flux density and spectral index at Band 4 adopted in the calibration script. The calibrator was observed at Bands 3, 6, and 7 within one week around the day when TW Hya was observed at Band 4. The flux density at each band estimated from the flux density and spectral index at Band 4 is consistent with the observed flux within an accuracy of greater than ∼95%, although the observed values are scattered around the fitting formula with a standard error of 4.5%–12%, which is larger at shorter wavelengths.

We used two project IDs for Band 6, both of which employed J1037–2934 as an amplitude calibrator. One project determined the flux density of the calibrator by observing a solar system object Pallas on the same day that TW Hya was observed. Therefore, the uncertainty due to the time variation of the calibrator flux density has little influence on the accuracy of the target flux density. However, there are still uncertainties originating from sources such as modeling of the atmosphere and the rotational effects of the solar system objects. Although these uncertainties are difficult to quantify, the uncertainty is typically ∼5% (see ALMA Technical Handbook). For the other execution block, Figure A3 shows the observed flux density of the calibrator at Band 6 before and after the day when TW Hya was observed. The flux density of the calibrator was measured nearly one week prior to the TW Hya observation and was almost constant with time. Although the flux densities observed three weeks after the TW Hya observation had relatively large errors, the adopted flux density is consistent with the value estimated from the fitting within an accuracy uncertainty of less than ∼5%.

Figure A4 shows the observed flux density of the calibrators at Band 7 around the observation date(s) of each observation project. For all of these observations, the flux density was measured at almost 10 days within the observation dates. The

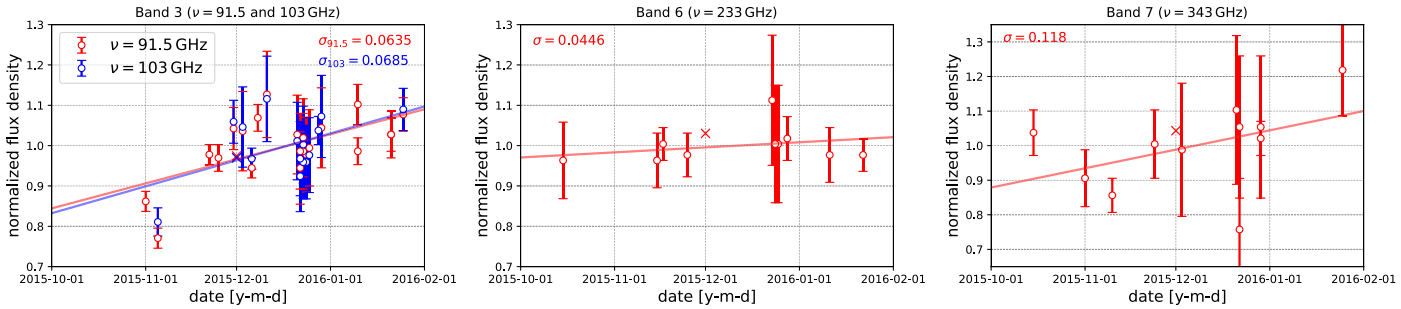

Figure A2. Time dependence of the flux of J1037–2934 at Bands 3 (left panel), 6 (middle panel), and 7 (right panel). The crosses correspond to the flux density estimated from the flux density and spectral index adopted in the calibration process. The solid lines denote the linear fitting of the observed flux densities. The flux is normalized by the average in each panel.

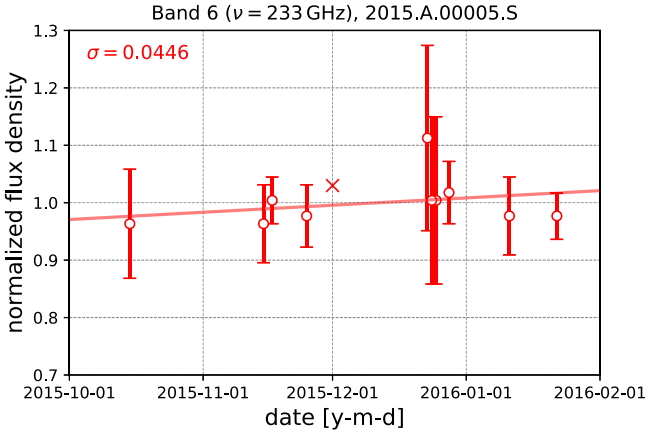

Figure A3. Time dependence of the flux of J1037–2934 at Band 6. The red circles show the flux density at $\nu = 233$ GHz. The solid line denotes the linear fitting of the observed flux densities. The crosses correspond to the flux density estimated from the flux density and spectral index used in the calibration process. The flux is normalized by the average.

flux density of the calibrator in observations of project ID 2015.1.00308.S significantly changes before and after the TW Hya observation (∼50%). To check the influence of this data, we made the combined Band 7 image using the data sets except for 2015.1.00308.S, and we confirmed that the variation of the total flux density of the image is only less than ∼1%. The flux density scatters around the fitting formula with a standard error of 4.4%–15%, and the adopted flux density is consistent with the flux density estimated from the fitting within an accuracy uncertainty of 15%.

The Band 9 observation employed J1037–2934 as an amplitude calibrator. The flux density of the calibrator was determined by observing Titan in the same execution block, which took off the uncertainty caused by the time variability of the calibrator as mentioned above.

From these analyses, we set the uncertainty as 10% for Bands 3, 4, and 6, 15% for Band 7, and 20% for Band 9, which are more conservative than the official values, and check the impact on our models. Figure A5 shows the intensities with different dust sizes with scattering for the same disk temperature and mass with the model shown Figure 7. We clearly see that the model with 300 μm-sized grains is still the best to reproduce the observed intensity profile. If the uncertainty is larger than 25% at Band 3, the model with 1 mm-sized grains would also be consistent with the observation. As shown in Section 4.6, the intensity difference between the models with and without scattering is more significant in shorter wavelengths for which scattering is negligible. If the uncertainty at Band 9 is less than 20%, the degeneracy between the models with and without scattering would be solved.

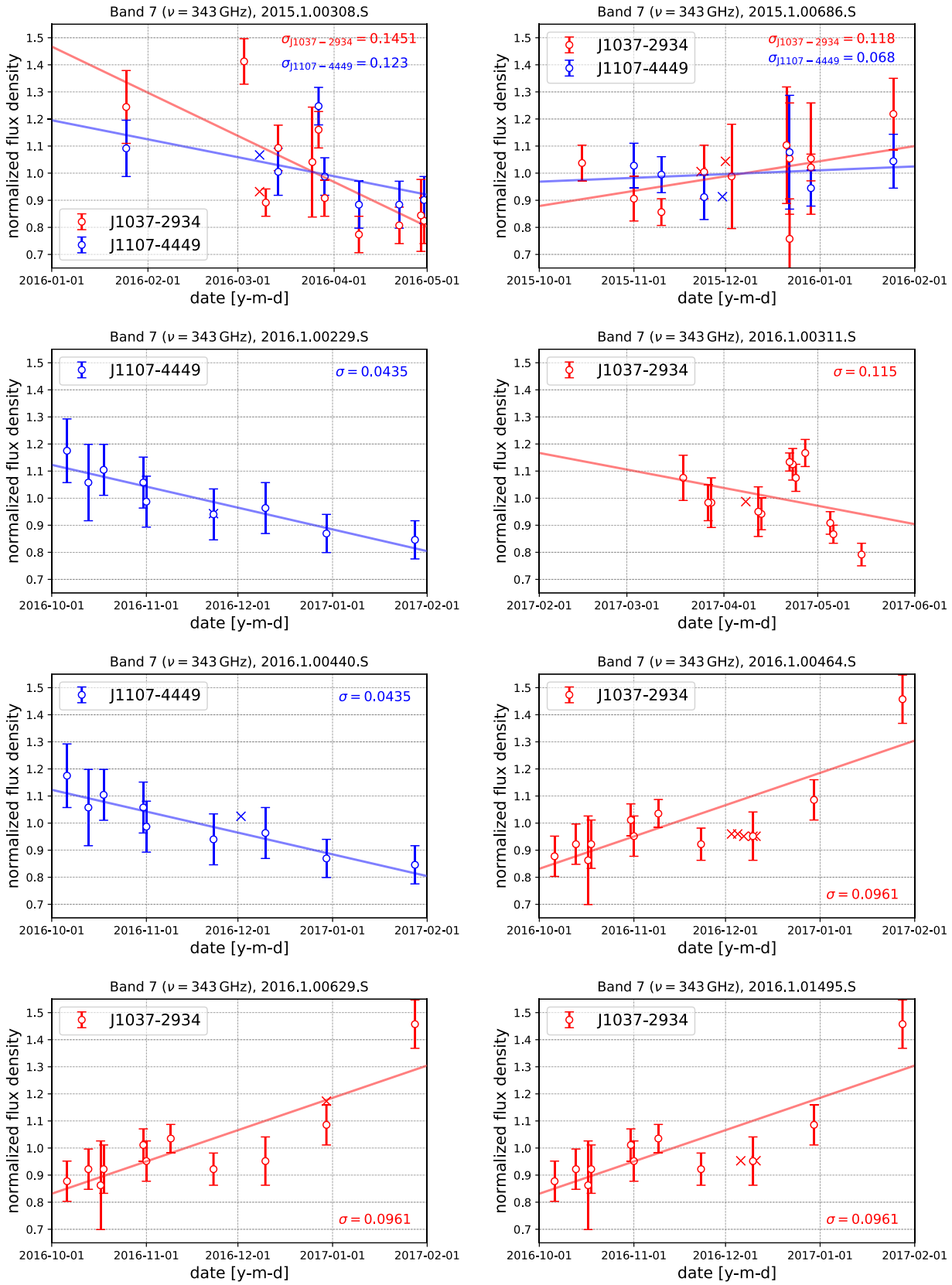

Figure A4. Time dependence of the flux of calibrators for each Band 7 observation. The red and blue circles show the flux density at $\nu = 343$ GHz for quasars J1037–2934 and J1107–4449, respectively. The red and blue solid lines denote the linear fitting of the observed flux densities of J1037–2934 and J1107–4449, respectively. The crosses correspond to the flux density estimated from the flux density and spectral index used in the calibration process. The flux is normalized by the average in each panel.

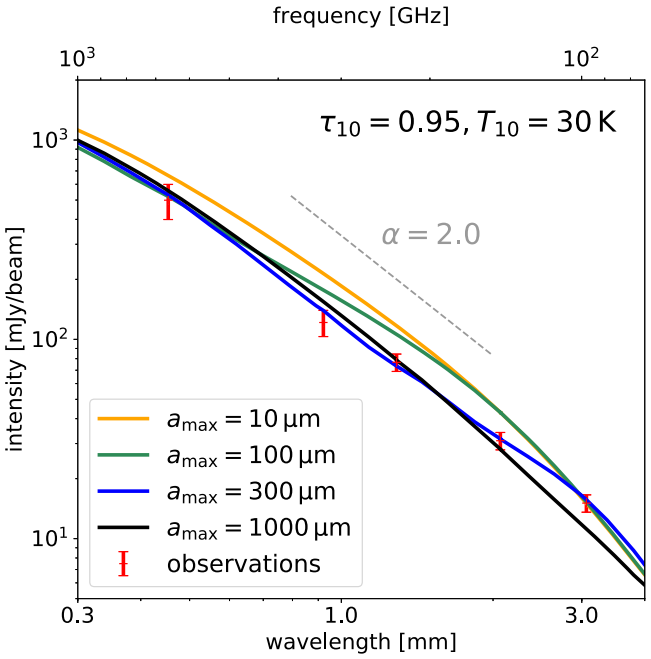

Figure A5. Same as Figure 7 but the uncertainty is set as 10% for Bands 3, 4, and 6, 15% for Band 7, and 20% for Band 9.

ORCID iDs

Takahiro Ueda https://orcid.org/0000-0003-4902-222X
Akimasa Kataoka https://orcid.org/0000-0003-4562-4119
Takashi Tsukagoshi https://orcid.org/0000-0002-6034-2892

References

Andrews, S. M., Huang, J., Pérez, L. M., et al. 2018, ApJL, 869, L41
Andrews, S. M., Rosenfeld, K. A., Kraus, A. L., & Wilner, D. J. 2013, ApJ, 771, 129
Andrews, S. M., & Williams, J. P. 2005, ApJ, 631, 1134
Andrews, S. M., Wilner, D. J., Zhu, Z., et al. 2016, ApJL, 820, L40
Ansdell, M., Williams, J. P., van der Marel, N., et al. 2016, ApJ, 828, 46
Bacciotti, F., Girart, J. M., Padovani, M., et al. 2018, ApJL, 865, L12
Beckwith, S. V. W., Sargent, A. I., Chini, R. S., & Guesten, R. 1990, AJ, 99, 924
Birnstiel, T., Dullemond, C. P., & Brauer, F. 2009, A&A, 503, L5
Birnstiel, T., Dullemond, C. P., Zhu, Z., et al. 2018, ApJL, 869, L45
Bohren, C. F., & Huffman, D. R. 1983, Absorption and Scattering of Light by Small Particles (New York: Wiley)
Calvet, N., D'Alessio, P., Hartmann, L., et al. 2002, ApJ, 568, 1008
Carrasco-González, C., Sierra, A., Flock, M., et al. 2019, ApJ, 883, 71
Carrera, D., Johansen, A., & Davies, M. B. 2015, A&A, 579, A43
Cieza, L. A., Ruíz-Rodríguez, D., Hales, A., et al. 2019, MNRAS, 482, 698
Dent, W. R. F., Pinte, C., Cortes, P. C., et al. 2019, MNRAS, 482, L29
Draine, B. T. 2003, ARA&A, 41, 241
Draine, B. T. 2006, ApJ, 636, 1114
Dullemond, C. P., Dominik, C., & Natta, A. 2001, ApJ, 560, 957
Dullemond, C. P., Juhasz, A., Pohl, A., et al. 2012, RADMC-3D: A Multi-purpose Radiative Transfer Tool (v0.41), Astrophysics Source Code Library, ascl:1202.015
Dullemond, C. P., & Monnier, J. D. 2010, ARA&A, 48, 205
Flaherty, K. M., Hughes, A. M., Teague, R., et al. 2018, ApJ, 856, 117
Gaia Collaboration, Brown, A. G. A., Vallenari, A., et al. 2016, A&A, 595, A2
Gundlach, B., & Blum, J. 2015, ApJ, 798, 34
Hayashi, C. 1981, in IAU Symp. 93, Fundamental Problems in the Theory of Stellar Evolution (Dordrecht: Reidel), 113
Henning, T., & Stognienko, R. 1996, A&A, 311, 291
Hogerheijde, M. R., Bekkers, D., Pinilla, P., et al. 2016, A&A, 586, A99
Huang, J., Andrews, S. M., Cleeves, L. I., et al. 2018a, ApJ, 852, 122
Huang, J., Andrews, S. M., Dullemond, C. P., et al. 2018b, ApJL, 869, L42
Hull, C. L. H., Yang, H., Li, Z.-Y., et al. 2018, ApJ, 860, 82
Kataoka, A., Muto, T., Momose, M., et al. 2015, ApJ, 809, 78
Kataoka, A., Muto, T., Momose, M., Tsukagoshi, T., & Dullemond, C. P. 2016a, ApJ, 820, 54
Kataoka, A., Okuzumi, S., Tanaka, H., & Nomura, H. 2014, A&A, 568, A42
Kataoka, A., Tsukagoshi, T., Momose, M., et al. 2016b, ApJL, 831, L12
Kim, S., Nomura, H., Tsukagoshi, T., Kawabe, R., & Muto, T. 2019, ApJ, 872, 179
Lin, M.-K. 2019, MNRAS, 485, 5221
Liu, H. B. 2019, ApJL, 877, L22
Liu, H. B., Vorobyov, E. I., Dong, R., et al. 2017, A&A, 602, A19
Lynden-Bell, D., & Pringle, J. E. 1974, MNRAS, 168, 603
Manara, C. F., Morbidelli, A., & Guillot, T. 2018, A&A, 618, L3
McMullin, J. P., Waters, B., Schiebel, D., Young, W., & Golap, K. 2007, in ASP Conf. Ser. 376, CASA Architecture and Applications, ed. R. A. Shaw, F. Hill, & D. J. Bell (San Francisco, CA: ASP), 127
Menu, J., van Boekel, R., Henning, T., et al. 2014, A&A, 564, A93
Min, M., Rab, C., Woitke, P., Dominik, C., & Ménard, F. 2016, A&A, 585, A13
Miyake, K., & Nakagawa, Y. 1993, Icar, 106, 20
Musiolik, G., Teiser, J., Jankowski, T., & Wurm, G. 2016, ApJ, 827, 63
Nomura, H., Tsukagoshi, T., Kawabe, R., et al. 2016, ApJL, 819, L7
Ohashi, S., Kataoka, A., Nagai, H., et al. 2018, ApJ, 864, 81
Okuzumi, S., & Tazaki, R. 2019, ApJ, 878, 132
Qi, C., Ho, P. T. P., Wilner, D. J., et al. 2004, ApJL, 616, L11
Rybicki, G. B., & Lightman, A. P. 1979, Radiative Processes in Astrophysics (New York: Wiley)
Stephens, I. W., Yang, H., Li, Z.-Y., et al. 2017, ApJ, 851, 55
Tazaki, R., & Tanaka, H. 2018, ApJ, 860, 79
Teague, R., Henning, T., Guilloteau, S., et al. 2018, ApJ, 864, 133
Thi, W. F., Mathews, G., Ménard, F., et al. 2010, A&A, 518, L125
Toomre, A. 1964, ApJ, 139, 1217
Tsukagoshi, T., Muto, T., Nomura, H., et al. 2019, ApJL, 878, L8
Tsukagoshi, T., Nomura, H., Muto, T., et al. 2016, ApJL, 829, L35
Ueda, T., Flock, M., & Okuzumi, S. 2019, ApJ, 871, 10
van Boekel, R., Henning, T., Menu, J., et al. 2017, ApJ, 837, 132
Wada, K., Tanaka, H., Okuzumi, S., et al. 2013, A&A, 559, A62
Warren, S. G., & Brandt, R. E. 2008, JGRD, 113, D14220
Woitke, P., Min, M., Pinte, C., et al. 2016, A&A, 586, A103
Yang, C.-C., Johansen, A., & Carrera, D. 2017, A&A, 606, A80
Youdin, A. N., & Goodman, J. 2005, ApJ, 620, 459
Zhang, K., Bergin, E. A., Blake, G. A., Cleeves, L. I., & Schwarz, K. R. 2017, NatAs, 1, 130
Zhu, Z., Zhang, S., Jiang, Y.-F., et al. 2019, ApJL, 877, L18
Zubko, V. G., Mennella, V., Colangeli, L., & Bussoletti, E. 1996, MNRAS, 282, 1321